



Structure-based discovery of potent WD repeat domain 5 inhibitors that demonstrate efficacy and safety in preclinical animal models

Kevin B. Teuscher^a, Somenath Chowdhury^a, Kenneth M. Meyers^a , Jianhua Tian^b , Jiqing Sai^a, Mayme Van Meveren^a, Taylor M. South^a, John L. Sensintaffar^a, Tyson A. Rietz^a, Soumita Goswami^c , Jing Wang^{d,e}, Brian C. Grieb^{c,f} , Shelly L. Lorey^c, Gregory C. Howard^c , Qi Liu^{d,e} , William J. Moore^g , Gordon M. Stott^h , William P. Tansey^{a,c} , Taekyu Lee^a, and Stephen W. Fesik^{a,i,j,1} 

Edited by Dale Boger, The Scripps Research Institute, La Jolla, CA; received July 1, 2022; accepted October 30, 2022

WD repeat domain 5 (WDR5) is a core scaffolding component of many multiprotein complexes that perform a variety of critical chromatin-centric processes in the nucleus. WDR5 is a component of the mixed lineage leukemia MLL/SET complex and localizes MYC to chromatin at tumor-critical target genes. As a part of these complexes, WDR5 plays a role in sustaining oncogenesis in a variety of human cancers that are often associated with poor prognoses. Thus, WDR5 has been recognized as an attractive therapeutic target for treating both solid and hematological tumors. Previously, small-molecule inhibitors of the WDR5-interaction (WIN) site and WDR5 degraders have demonstrated robust *in vitro* cellular efficacy in cancer cell lines and established the therapeutic potential of WDR5. However, these agents have not demonstrated significant *in vivo* efficacy at pharmacologically relevant doses by oral administration in animal disease models. We have discovered WDR5 WIN-site inhibitors that feature bicyclic heteroaryl P₇ units through structure-based design and address the limitations of our previous series of small-molecule inhibitors. Importantly, our lead compounds exhibit enhanced on-target potency, excellent oral pharmacokinetic (PK) profiles, and potent dose-dependent *in vivo* efficacy in a mouse MV4:11 subcutaneous xenograft model by oral dosing. Furthermore, these *in vivo* probes show excellent tolerability under a repeated high-dose regimen in rodents to demonstrate the safety of the WDR5 WIN-site inhibition mechanism. Collectively, our results provide strong support for WDR5 WIN-site inhibitors to be utilized as potential anticancer therapeutics.

WDR5 | MYC | structure-based design | *in vivo* efficacy | cancer therapy

WD repeat domain 5 (WDR5) is a member of the WD40-repeat protein family and performs a variety of critical chromatin-centric processes in the nucleus by serving as a core scaffolding component of many multiprotein complexes (1–9). Overexpression of WDR5 is observed in a variety of aggressive solid and hematological cancers, such as bladder (10), breast (11), colorectal (12), gastric (13), pancreatic (14), prostate (15, 16), neuroblastoma (17), head neck squamous cell carcinoma (18), liver (19), and various leukemias (20, 21), and is often associated with poor prognoses (11, 18, 21). WDR5 utilizes two major binding interfaces, the WDR5 interaction motif (WIN) and WDR5-binding motif (WBM), on opposite sides of its circular barrel-shaped structure to assemble multiprotein complexes (22–24). For example, WDR5 interacts with the MLL/SET (MLL1–4, SETd1A, and SETd1B) family of histone methyltransferase (HMT) complexes, which catalyze histone H3 lysine 4 (H3K4) di- and tri-methylation (H3K4me2, me3) (4–6, 8, 25–29). An HMT complex is composed of a functional subunit, such as MLL1, which is anchored to the WDR5 WIN site via a conserved arginine residue. In addition, other conserved partner proteins, including RBBP5, ASH2L, and DPY30 bind to WDR5 through WIN-site independent interactions. Indeed, MLL-fusion cancer cells demonstrate a strong empirical sensitivity to WIN-site inhibitors (30). Additionally, WDR5 has been identified as an essential cofactor for MYC-promoted tumorigenesis. WDR5 scaffolds the association of MYC to chromatin at tumor-critical target genes through utilization of both the WIN and WBM sites. While tethered to chromatin via the WIN site, WDR5 recruits MYC proteins through a direct interaction between the WDR5 WBM site and the conserved MYC Box IIIb element within the MYC central portion (31–33). The exchange of wild-type c-MYC for a mutant with impaired WBM binding caused rapid tumor regression and loss of oncogenic potential in an *in vivo* model and supported WDR5 as a therapeutic target to inhibit MYC-mediated malignant gene expression (33). This result also suggests that blockade of either the WDR5 WIN or WBM sites may achieve similar levels of MYC inhibition by preventing colocalization of the WDR5–MYC

Significance

WD repeat domain 5 (WDR5) is a component of multiprotein complexes in the nucleus that sustain oncogenesis in human cancers. Previously reported WDR5 inhibitors and degraders reduce the proliferation of cancer cell lines and established the utility of WDR5 as an anticancer strategy. However, these agents have only achieved modest cancer tumor growth inhibition in animal models due to their suboptimal druglike properties. We report the discovery of a series of potent WDR5-interaction (WIN)-site inhibitors with improved druglike properties that demonstrate significant *in vivo* antitumor efficacy and safety in animal models. Our results support the further development of WDR5 WIN-site inhibitors as anticancer therapeutics.

Competing interest statement: The authors have patent filings to disclose. The authors declare the following competing interest: K.B.T., S.C., K.M.M., J.T., T.L., and S.W.F. are inventors on a patent application that was filed to protect this series of WDR5 inhibitors. “WDR5 Inhibitors and Modulators” WO2021092525A1, pending. All other authors declare no competing interest.

This article is a PNAS Direct Submission.

Copyright © 2022 the Author(s). Published by PNAS. This article is distributed under Creative Commons Attribution-NonCommercial-NoDerivatives License 4.0 (CC BY-NC-ND).

¹To whom correspondence may be addressed. Email: Stephen.fesik@vanderbilt.edu.

This article contains supporting information online at <https://www.pnas.org/lookup/suppl/doi:10.1073/pnas.2211297120/-/DCSupplemental>.

Published December 27, 2022.

complex on chromatin or directly inhibiting MYC and WDR5 binding, respectively. Therefore, inhibition of WDR5 may be an effective therapeutic option against a broad range of tumors, including MLL-rearranged leukemias and MYC up-regulated cancers (1, 7, 31, 34–41).

Substantial progress has been made toward the discovery of WDR5 WIN-site inhibitors. Early prototypes, such as the macrocyclic peptidomimetic inhibitor MM-589 (35) and the small-molecule inhibitor OICR-9429 (36, 42), demonstrated the mechanistic proof-of-concept through successful target engagement in *in vitro* assays (Fig. 1). Furthermore, they exhibited mild antiproliferative activities in WDR5-sensitive cancer cells (35, 36, 42). We have also reported the discovery of highly potent WDR5 WIN-site inhibitors that were obtained using fragment-based methods and structure-based design (41, 43–45). Our early small-molecule probes C6 (44) and C16 (41) are highly potent WDR5 inhibitors that display robust antiproliferative activity against the MV4:11 cell line and have been utilized to investigate the cellular effect of WIN-site inhibition. These probes rapidly displaced WDR5 from chromatin and triggered transcriptional repression of WDR5-bound ribosome protein genes, which caused dose-dependent p53 induction and led to p53-dependent apoptosis (41, 44). Furthermore, WIN-site inhibitors, such as C16, successfully remove MYC from MYC/WDR5 cobound target genes by displacing WDR5 from chromatin and exhibited potent antiproliferative effects in the MYC-driven cancer cell line CHP-134 (neuroblastoma) (41, 44). These observations support the tremendous therapeutic potential of WDR5 WIN-site inhibitors that target the tumorigenic function of MYC by blocking the recruitment of MYC to a key set of protein synthesis genes on chromatin (41).

The efficacy and toxicity of a WDR5-targeted therapy have been predicted based on RNAi-mediated knockdown and CRISPR gene knockout studies (36–38). WDR5 is panessential (46, 47), and its depletion has profound global effects on cellular transcription levels and phenotypic outcomes. Selective therapeutic strategies that only affect a subset of WDR5's functions are necessary to reduce potential on-target toxicity. WDR5 proteolysis-targeting chimeras (PROTACs) have been developed and rely on the

pharmacological degradation of WDR5 to achieve efficacy. The advanced WDR5 PROTAC MS67 (Fig. 1) demonstrated significant degradation of WDR5 in cells and *in vivo* tumor growth inhibition (TGI) in mouse models (48). This result may be appropriately considered in connection with the knockdown studies because the therapeutic effect of a WDR5 PROTAC is dependent on the depletion of WDR5. In contrast, a recent study indicated that the WIN-site inhibitor C16 affected only a subset of WDR5-regulated gene expression compared with acute depletion of WDR5 by an auxin-inducible degron in engineered Ramos cells (49). This result suggests that the therapeutic potential and on-target-mediated toxicity of the WDR5 WIN-site inhibition mechanism may be different from the WDR5 PROTAC approach and needs to be evaluated in *in vivo* efficacy and safety models using a selective WIN-site blocker.

The pharmacological effect of WDR5 WIN-site inhibition relies on the sustained blockade of the WIN site and requires 3 to 5 d of incubation to deliver a robust antiproliferative effect in *in vitro* cellular assays (41). Consequently, repeated doses of a potent WIN-site inhibitor would be necessary to maintain a pharmacologically relevant systemic exposure to be efficacious in animal disease models. To be considered as a therapeutic agent, a WDR5 WIN-site inhibitor requires extremely high on-target potency to achieve an effective target engagement at lower compound concentrations. In addition, a suitable pharmacokinetic (PK) profile with low clearance and high oral bioavailability would be desirable to increase the duration of the pharmacological effect and utilize a favorable route of administration under a daily dosing regimen. However, there have been no reported WDR5 inhibitors or PROTACs that achieve significant *in vivo* efficacy at a pharmacologically relevant dose by oral administration in preclinical cancer models. Recently, we discovered a series of highly potent and orally bioavailable WDR5 WIN-site inhibitors using a pharmacophore-based optimization method (45). Here, we report our continued efforts to further optimize the potency, druglike properties, and PK profiles of WDR5 WIN-site inhibitors. Finally, the therapeutic potential and on-target-mediated toxicity of the WDR5 WIN-site inhibition mechanism were evaluated by using these probes in *in vivo* efficacy and safety studies.

Results

Structure-Based Design of the Bicyclic Heteroaryl P₇ Pharmacophore Unit. We recently reported a class of WDR5 WIN-site inhibitors that exhibited high on-target potency, improved physicochemical properties, and good oral PK profiles (45). The structure of representative compound **1** (Fig. 2A) was divided into four pharmacophore units (P₂, P₄, P₇, and core) according to their binding subsite alignments in the WIN site with residues 3,764 to 3,773 (ARAEVHLRKS) of MLL1 (50). The X-ray cocrystal structure of compound **1** bound to WDR5 (Fig. 2B) revealed that the conformationally rigid 3,4-dihydroisoquinolin-1(2*H*)-one core forms a critical hydrogen bond (H-bond) between the carbonyl oxygen of **1** and the backbone amide NH of C261 and a T-shaped π - π stacking interaction with F133. The anchored core provides the appropriate exit vectors for the P₂, P₄, and P₇ pharmacophore units to extend to the S₂, S₄, and S₇ binding subsites, respectively (Fig. 2C) (41, 45). Both *N*-linked imidazole and 2-methyl imidazole are P₂ pharmacophore units that form the critical sandwiched π - π stacking interactions with WDR5 residues F133 and F263 in the S₂ subsite (Fig. 2D). Importantly, compounds containing the imidazole P₂ unit are orally bioavailable and well-tolerated in mice even at high doses. The 1-methyl or 1-ethyl-3-(trifluoromethyl)-1*H*-pyrazol P₄, and properly substituted 2-pyridylmethyl P₇ pharmacophore units

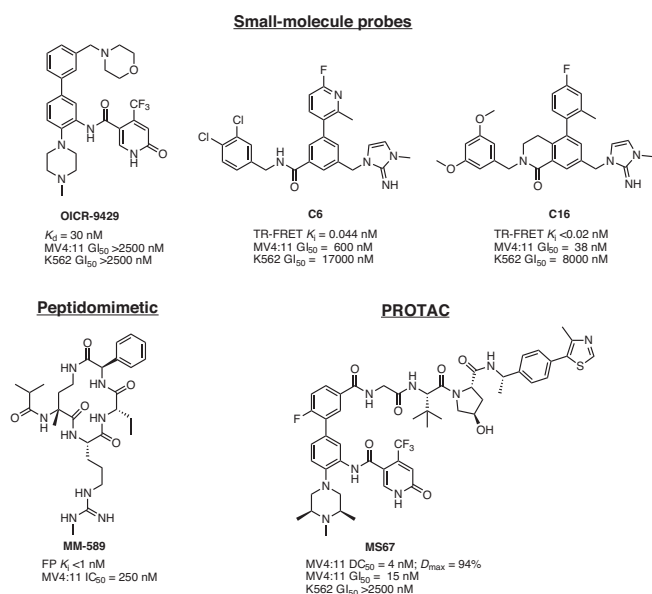


Fig. 1. Chemical structures and *in vitro* profiles of representative WDR5 WIN-site inhibitors and WDR5 PROTAC.

bind in the S_4 and S_7 subsites (Fig. 2 *E* and *F*), respectively, to enhance both the on-target potency and physicochemical properties. The metabolic stability of the compounds was improved when α -substituted 2-pyridylmethyl P_7 units were introduced resulting in an improved in vivo PK profile. While approximately half of the P_7 unit binds in the S_7 subsite, the remaining portion is solvent exposed and provides an ideal region for further property optimization of the compounds without significantly affecting the key binding interactions. Although α -substituted 2-pyridylmethyl P_7 units offer multiple desirable attributes, the derivatization of the unit is limited due to the synthetic accessibility of optically pure P_7 building blocks.

To further optimize our WDR5 WIN-site inhibitors, new P_7 units were designed based on the WDR5 bound conformation of the (*S*)-1-cyclopropyl-1-(4-methylpyridine-2-yl)methyl P_7 unit of compound **1** (Fig. 2*G*) (45). The 4-methylpyridine-2-yl group is positioned above the Y191 residue, which engages in a parallel-displaced π - π stacking interaction along the floor of the S_7 subsite and adopts a perpendicular conformation to the 3,4-dihydroisoquinolin-1(2*H*)-one core of **1**. Conversely, the (*S*)-cyclopropyl group is positioned completely out of the pocket and rotated away from the P_7 and core units. Therefore, we hypothesized that the rearrangement of the (*S*)-cyclopropyl group through ring opening and cyclization to the 4-methylpyridine-2-yl ring forms a bicyclic heteroaryl P_7 unit that may preserve the original binding conformation of the (*S*)-1-cyclopropyl-1-(4-methylpyridine-2-yl)methyl P_7 unit of **1**. The formation of the new bicyclic heteroaryl P_7 unit removes one rotatable bond from the P_7 unit of **1** and reduces the conformational flexibility of the WIN-site inhibitor. Additionally, the extended π -network of the bicyclic heteroaryl P_7 unit may strengthen the π - π stacking interaction with Y191. Consequently, this P_7 unit may further enhance the on-target potency of this series of WIN-site inhibitors. Furthermore, this structural modification also eliminates the metabolically vulnerable benzylic methylene of the monocyclic P_7 series (45), which may reduce the systemic clearance and improve the oral bioavailability of the bicyclic heteroaryl P_7 series inhibitors. Finally, development of this series would benefit from the improved synthetic accessibility of bicyclic heteroaryl halides, which were directly purchased or rapidly synthesized from commercially available building blocks. To demonstrate the benefits of the bicyclic heteroaryl P_7 unit, we conducted a focused structure-activity relationship (SAR) study using a convergent synthetic strategy. A variety of bicyclic heteroaryl P_7 units were efficiently installed through late-stage Buchwald cross-coupling with previously reported advanced lactam intermediates (45) to produce a focused library of around 230 WDR5 WIN-site inhibitors (51) (Fig. 2*H*).

On-target potency of this series of inhibitors was accessed using a time-resolved fluorescence energy transfer (TR-FRET) assay and cell proliferation assays with WDR5-sensitive cell lines MV4:11 and MOLM-13, and WDR5-resistant K562 cells (41, 45). The half-maximal growth inhibition (GI_{50}) ratio between K562 and MV4:11 was used as a cellular selectivity measure (40, 42). In general, these inhibitors exhibited excellent WDR5-mediated on-target potency and desirable physicochemical properties. The in vivo PK profiles of inhibitors that met cellular potency criteria were determined in mice. Compounds bearing quinolin-4-yl or quinolin-5-yl P_7 analogs delivered superior oral PK properties with low clearance rates and high oral bioavailability. Here, we report a representative set of WDR5 WIN-site inhibitors that led to the discovery of in vivo probes **3**, **9**, and **10**.

The in vitro on-target potency and physicochemical properties of compounds **3** to **10** are summarized in Table 1 along with the previously reported monocyclic P_7 analog **2** for comparison (45). The nitrogen of the 2-pyridylmethyl P_7 of **1** was repositioned to allow

the formation of the second ring at that position. The resulting compounds **3** to **5** containing quinolinyl or isoquinolinyl P_7 units were profiled early in the SAR development and served as benchmarks. Compound **3** with the 3-methoxyquinolin-5-yl P_7 unit bound tightly to the WDR5 WIN site (Table 1) with a $K_i = 20$ pM, which was the theoretical detection limit of the TR-FRET assay. Compound **3** also exhibited potent WDR5 inhibition-mediated cellular efficacy against MLL-rearranged cancer cell lines MV4:11 and MOLM-13. Even though **3** was an early prototype for this series, it exhibited similar WDR5-binding affinity and antiproliferative activities in the sensitive cell lines compared with the refined monocyclic analog **2**. Intriguingly, compound **3** was significantly less cytotoxic in WDR5-resistant K562 cells and improved the on-target cellular selectivity by 4.6-fold over **2**. This result suggests that the bicyclic heteroaryl P_7 unit may reduce the off-target activities that were present in the monocyclic analog. When the nitrogen was repositioned to the extended ring to form the 6-methoxyquinolin-4-yl and 6-methylisoquinolin-4-yl P_7 units, the antiproliferative activities of **4** and **5** were marginally reduced by twofolds. The potency was regained by the addition of methoxy or *N*-methylcarboxamide groups at the 8-position of the 6-methoxyquinolin-4-yl P_7 unit. Consequently, compounds **6** and **7** showed comparable on-target potency and cellular selectivity to **3**. Interestingly, the potency of compound **8** bearing the *N,N*-dimethylcarboxamide was significantly reduced compared to the *N*-methylcarboxamide analog **7**. The potency of the series was further optimized by substituting a 6-ethyl for the 6-methoxy group of the quinolin-4-yl P_7 unit. Fully optimized compounds **9** and **10** exhibited binding affinities below the limit of quantitation for the TR-FRET assay and the highest antiproliferative activity with $GI_{50} < 10$ nM in MV4:11 cells. It is also noteworthy that the bicyclic heteroaryl P_7 series of potent WDR5 WIN-site inhibitors maintained higher cellular selectivity compared with the monocyclic analog **2**. These results validated our structure-based design strategy.

The physicochemical properties of **3** to **10** were profiled to assess how the bicyclic heteroaryl P_7 units affect the druglike character of these WIN-site inhibitors (Table 1). Generally, compounds with a bicyclic heteroaryl P_7 unit had an increased kinetic aqueous solubility compared with **2**. Compounds **3** to **10** appeared to have sufficiently high aqueous solubility to facilitate oral absorption. The nonspecific plasma protein binding of **2** to **10** was assessed using an in vitro mouse whole-blood protein-binding (WBPB) assay. This parameter provides context to compare the in vivo PK profile and the observed therapeutic effect of the compound in in vivo animal disease models. At a concentration of 1 μ M, compound **2** showed extremely high protein binding with only a 0.2% unbound free fraction in mouse whole blood. Generally, the unbound fractions of the bicyclic heteroaryl P_7 series were significantly higher than **2**. Although compound **10** showed the highest protein binding within the series, the unbound fraction (0.4%) was still a twofold increase compared with **2**. Overall, these results suggest that bicyclic heteroaryl P_7 units improve the druglike properties of WIN-site inhibitors.

The X-ray cocrystal structure of **10** bound to WDR5 was obtained to understand the binding interactions and conformation of the 6-ethyl-*N*-methylquinoline-8-carboxamide P_7 unit. Compound **10** bound in the WDR5 WIN site by accessing all binding subsites (Fig. 3*A*). As expected, the 3,4-dihydroisoquinolin-1(2*H*)-one core, imidazole P_2 , and 1-methyl-3-(trifluoromethyl)-1*H*-pyrazole-4-yl P_4 units engaged all critical binding interactions found in the X-ray structure of **1** bound to WDR5 (Fig. 3*B*). The 6-ethyl-*N*-methylquinoline-8-carboxamide P_7 unit was positioned above Y191 to form a parallel-displaced π - π

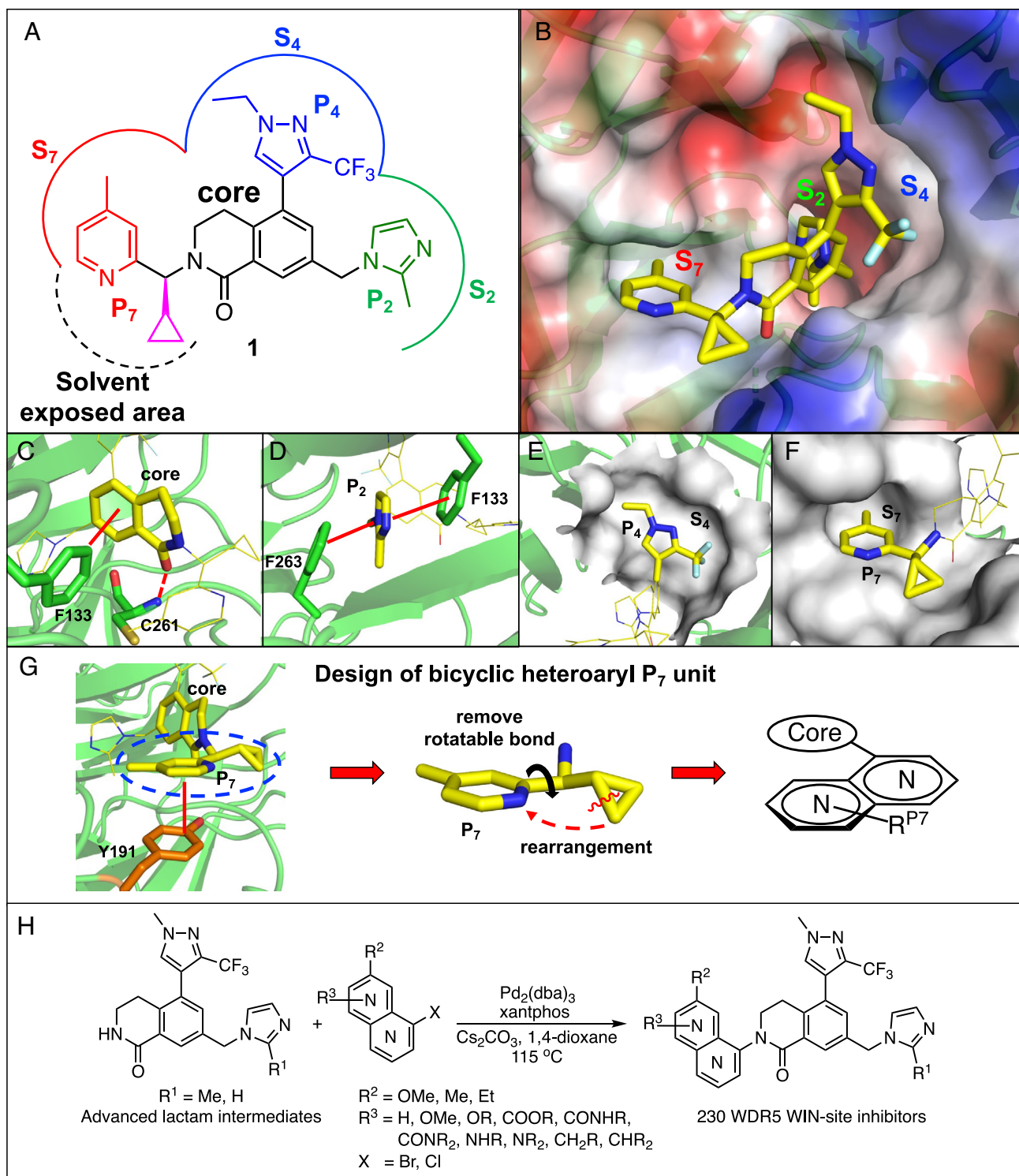
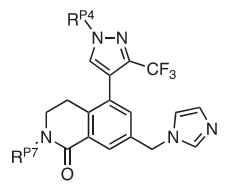
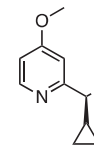
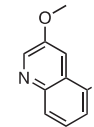
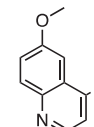
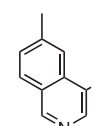
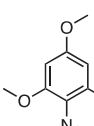
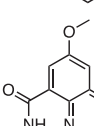
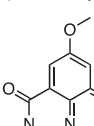
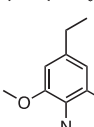
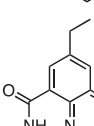


Fig. 2. Discovery of WDR5 WIN-site inhibitors containing a bicyclic heteroaryl P₇ unit. (A) The structure of **1** from monocyclic P₇ series of WDR5 WIN-site inhibitors with labeled pharmacophore units (P₂, P₄, and P₇), binding subsites (S₂, S₄, and S₇), and solvent exposed area. (B) X-ray cocrystal structure of **1** (yellow carbon-capped sticks) bound to WDR5 (PDB ID: 7UAS) with labeled S₂, S₄, and S₇ binding subsites. (C) Key H-bond (red dashed lines) and π - π stacking interactions (red solid lines) of the core (yellow sticks) with WDR5 residues C261 and F133 (green sticks), respectively. (D) Key π - π stacking interactions (red lines) of the P₂ unit (yellow sticks) with WDR5 residues F133 and F263 (green sticks). (E) Binding conformation of the P₄ unit (yellow sticks) in the S₄ subsite (gray surface). (F) Binding conformation of the α -substituted monocyclic P₇ unit (yellow sticks) in the S₇ subsite (gray surface). (G) Structure-based design of bicyclic heteroaryl P₇ units using the X-ray cocrystal structure of **1** (PDB ID: 7UAS) as a model. (H) Convergent synthesis of WDR5 WIN-site inhibitors using late-stage Buchwald coupling of advanced lactam intermediates (45) and bicyclic heteroaryl P₇ units.

stacking interaction in the S₇ subsite (Fig. 3C). The 6-ethyl group bound in the deepest part of S₇ subsite, while the *N*-methyl 8-carboxamide was positioned in the solvent accessible area of the WDR5 WIN site. The quinoline portion of the P₇ unit also

adopted a perpendicular conformation to the 3,4-dihydroisoquinolin-1(2*H*)-one core, which was consistent with the original design strategy. Finally, the overlay of WDR5 bound conformations of the core, P₂, and P₄ units in **1** and **10** (Fig. 3D) were nearly

Table 1. In vitro on-target potency and physicochemical properties of compounds 2 to 10


Compound	R ^{P4} =	R ^{P7} =	TR-FRET K _i (nM) [*]	Cell proliferation assays GI ₅₀ (nM) [*]			Selectivity [†]	Kinetic solubility [‡]	Mouse WBPB [§]
			WDR5	MV4:11	MOLM-13	K562	K562/ MV4:11	pH 7.4 (μM)	%
2[¶]	Et		<0.02	19 ± 5.2	37 ± 8.1	1,500 ± 860	79	55	99.8 ± 0.1
3	Me		0.020 ± 0.003	17 ± 7.4	54 ± 9.6	6,200 ± 6,500	360	73	97.8 ± 0.2
4	Me		<0.02	45 ± 5.6	95 ± 22	13,000 ± 5,000	290	73	98.7 ± 0.3
5	Me		0.028 ± 0.006	42 ± 8.3	73 ± 16	4,900 ± 2,500	120	70	98.6 ± 0.3
6	Me		0.025 ± 0.01	18 ± 8.7	33 ± 5.1	7,300 ± 1,300	410	68	96.5 ± 0.4
7	Me		0.021 ± 0.004	23 ± 9.5	30 ± 9.1	9,700 ± 7,000	420	73	98.7 ± 0.2
8	Me		0.043 ± 0.01	420 ± 120	2,300 ± 150	>30,000	>70	95	85.7 ± 1.6
9	Me		<0.02	9.2 ± 4.0	31 ± 6.7	2,200 ± 980	240	62	98.7 ± 0.2
10	Me		<0.02	9.7 ± 5.0	32 ± 6.0	2,500 ± 1,800	260	31	99.6 ± 0.0

^{*}TR-FRET K_i and cell proliferation GI₅₀ values are the mean ± SD (n = 4).

[†]Selectivity is defined as GI_{50, K562}/GI_{50, MV4:11} and is used to generally distinguish between on- and off-target inhibition mechanisms.

[‡]Kinetic aqueous solubility was tested at a compound concentration of 100 μM and the reported values represent the mean (n = 2).

[§]Mouse whole-blood protein binding (WBPB) was tested at a compound concentration of 1 μM and the reported values represent the mean ± SD (n = 3).

[¶]The potency and kinetic aqueous solubility data for **2** were reported previously (45).

superimposable. The 6-ethyl-*N*-methylquinoline-8-carboxamide P₇ unit of **10** filled the same binding space as the (*S*)-1-cyclopropyl-1-(4-methylpyridine-2-yl)methyl P₇ unit of **1** in the S₇ subsite.

Compound 3 Displays Favorable PK Properties and Demonstrates Proof-Of-Concept In Vivo TGI. To select a probe for in vivo efficacy studies, the PK properties of compounds that met

potency (TR-FRET K_i < 30 pM, MV4:11 GI₅₀ < 50 nM) and physicochemical property (solubility >10 μM) criteria were evaluated in CD-1 mice. In vitro antiproliferative activity trends suggest that a sustained pharmacologically relevant occupancy of the WDR5 WIN site through repeated doses of an inhibitor would be essential to deliver robust in vivo efficacy. Thus, we emphasized selecting compounds that provide sufficient systemic

exposure (area under the plasma concentration-time curve ($t = 0$ –last timepoint), $AUC_{0\text{--last}}$) at pharmacologically relevant doses by oral administration. The monocyclic P_7 analog **2** was used as a reference and compounds **3** to **5** served as benchmarks for the more refined compounds of the bicyclic heteroaryl P_7 series. Systemic clearance rates of these compounds were measured at 3 mg/kg via intravenous (i.v.) administration and oral exposures were determined by oral (p.o.) administration at 10 and 50 mg/kg. The plasma concentrations of each compound were monitored for 24 h (SI Appendix, Fig. S1 B–F). The reference compound **2** showed low i.v. clearance ($Q_h < 25\%$) with dose-dependent linear exposures at the two oral dose levels with $\sim 45\%$ bioavailability. Compound **3** showed a similar i.v. clearance and oral exposure ($AUC_{0\text{--last}}$) compared with **2** at the 10 mg/kg dose with 57% oral bioavailability (Fig. 4A). When dosed at 50 mg/kg p.o., compound **3** exhibited a 2.6-fold increased dose-normalized exposure ($AUC_{0\text{--last}}/\text{dose}$) compared with the 10 mg/kg dose level with $>100\%$ oral bioavailability (as estimated from the 3 mg/kg i.v. dose). The PK profile of compound **4** also exhibited the similar nonlinear systemic oral exposure pattern found in **3** with a slightly higher i.v. clearance and lower oral exposure ($AUC_{0\text{--last}}$). Compound **5** showed the lowest clearance among the three benchmark compounds with a decreased nonlinear oral exposure pattern. Interestingly, the peak plasma concentration (C_{max}) of **5** was twofold lower than **3** at the 50 mg/kg p.o. dose and resulted in lower systemic exposure and oral bioavailability. The nonlinear increase in oral exposure for **3** to **5** may have resulted from a more efficient absorption at the high dose due to saturation of metabolism in the GI-tract and first pass effect in the liver. In addition, major systemic clearance mechanisms for these compounds may become saturated at high plasma concentrations. As a result, compound **3** had 2.5-fold higher oral exposure compared with the monocyclic P_7 analog **2**, when dosed at 50 mg/kg, despite both compounds showing similar PK profiles at the 10 mg/kg dose. Based on these data, **3** was selected as the first in vivo probe to demonstrate proof-of-concept WDR5 inhibition-mediated efficacy in a mouse xenograft tumor model. To achieve the highest level of systemic exposure for the pilot in vivo efficacy study, **3** was also dosed by intraperitoneal injection (i.p.) at 10, 50, and 100 mg/kg (SI Appendix, Fig. S1

G and H). At the 50 mg/kg dose level, **3** showed 1.5-fold higher exposure via i.p. administration than the p.o. group. In addition, compound **3** showed a linear dose-dependent plasma exposure by i.p. administration with longer sustainability. Compound **3** was also well-tolerated in a 5-d dose-escalation tolerability study by daily (QD) i.p. administration with no clinical abnormalities at the highest dose level (SI Appendix, Fig. S2). Therefore, a proof-of-concept WDR5-mediated TGI study in the mouse MV4:11 xenograft model was conducted via i.p. administration of **3**.

Compound **3** was dosed at 50, 75, and 100 mg/kg QD for 21 d via i.p. administration to female BALB/c nude mice bearing MV4:11 subcutaneous tumors to demonstrate in vivo TGI. Treatment began 10 d after tumor inoculation when the mean initial tumor volumes were 149 mm³. Compound **3** caused significant TGI in all dose groups compared with the vehicle control in a dose-dependent manner (Fig. 4B). The efficacy achieved by **3** was marginal during the first 4 d of dosing for all groups. Following this latency period, a significant delay in tumor growth began to be observed, and the most robust inhibitory effects were observed between days 5 and 14. The average tumor volumes for the 75 and 100 mg/kg dose groups regressed to the initial volume and were maintained during the period. The observed early delay in in vivo efficacy by WDR5 inhibition was consistent with the in vitro cellular antiproliferation pattern, which requires at least 3 d of incubation to deliver a robust antiproliferative effect. This result also confirms that a small-molecule WDR5 inhibitor requires prolonged target occupancy to exert its maximum anti-cancer effect. During the third week of dosing, the inhibitory effect of **3** subsided, and tumors began to grow at a faster rate, which may suggest the cancer cells developed resistance mechanisms against the treatment. Overall, compound **3** exhibited 56, 72, and 75% TGI in the 50, 75, and 100 mg/kg dose groups after 21 d of treatment compared with the vehicle control, respectively. Compound **3** was well-tolerated by the mice at all dose levels without any sign of clinical abnormalities or significant loss in body weight in the treated groups compared with the vehicle control group (Fig. 4C). To correlate the PK of **3** in plasma and tumor, a satellite group of MV4:11 xenografted mice ($n = 5$) was treated with a single 100 mg/kg dose by i.p. administration. The plasma and tumor concentrations of **3** were measured at 6, 18, and 24 h post-dose. Compound **3** maintained high plasma ($9,926 \pm 4,545$ ng/mL) and tumor ($23,312 \pm 5,597$ ng/g) concentrations at 6 h post-dose but showed near baseline exposures beyond 18 h in both compartments. This PK profile indicated that **3** was distributed ~ 2.3 -fold higher to the tumor compared with plasma during the elimination phase and completely cleared in 24 h. The exposure profile of **3** suggested that it is essential for WDR5 WIN-site inhibitors to maintain high daily exposure for at least 6 h to ensure in vivo efficacy. Finally, the PK data of **3** served as a benchmark to devise a target exposure-based dosing strategy for follow-up in vivo efficacy studies by p.o. administration.

Compounds **9** and **10** Demonstrate Robust In Vivo Antitumor Efficacy by Oral Administration.

Considering the results of the in vivo efficacy study with **3**, we selected more refined oral probes for follow-up studies based on oral systemic exposure. Compounds **6**, **7**, **9**, and **10** had increased oral bioavailability and exposure in CD-1 mice following i.v. (3 mg/kg) and p.o. (50 mg/kg) administration and were well-tolerated with no reported clinical abnormalities (SI Appendix, Fig. S3). Despite having high clearance, the oral exposure ($AUC_{0\text{--last}}$) of **6** was twofold higher than the parent compound **4** (Fig. 5A). The 8-*N*-methylcarboxamide substituted P_7 unit provided a significant

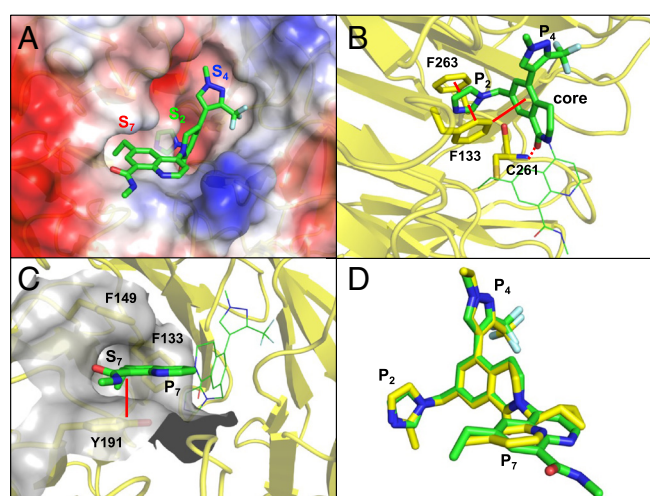


Fig. 3. X-ray cocrystal structure of compound **10** bound to WDR5. (A) X-ray cocrystal structure of **10** (green carbon-capped sticks) bound to WDR5 (PDB ID: 8E9F) with labeled S_2 , S_4 , and S_7 binding subsites. (B) Key H-bond (red dashed line) and π - π stacking interactions (red solid lines) of the core and P_2 units (green sticks) with WDR5 residues F133, C261, and F263 and bound conformation of the P_4 unit for **10**. (C) Binding conformation of the P_7 unit (green sticks) in the S_7 subsite (gray surface) with labeled S_7 side chain residues (yellow sticks). (D) Overlay of **1** (yellow sticks; PDB ID: 7UAS) and **10** (green sticks).

improvement in PK properties. Indeed, compound **7** exhibited lower i.v. clearance, a 5.2-fold higher oral C_{max} , and a 4.3-fold higher oral AUC_{0-last} compared with parent compound **4**. Compounds **9** and **10** containing 6-ethyl-quinolin-4-yl P_7 units exhibited the best overall in vitro on-target potency and in vivo PK profiles. Both compounds quickly reached their C_{max} within 1 h and maintained plasma concentrations above 1 μ M for 8 h following a single p.o. dose at 50 mg/kg. The total oral plasma exposure (AUC_{0-last}) of **9** and **10** increased by twofold compared with the initial probe **3** at the same dose level (Fig. 5A). Finally, both compounds exhibited a dose-proportional increase in systemic exposure up to 150 mg/kg by p.o. administration with an extended mean residency time (MRT) (SI Appendix, Fig. S3 C and D). Based on the improved cellular potency and oral PK profiles, compounds **9** and **10** were selected as probes for follow-up in vivo efficacy studies.

Compounds **9** and **10** were tested in the mouse MV4:11 subcutaneous xenograft model at 50, 100, and 150 mg/kg QD via p.o. administration for 21 d (Fig. 5 B and D). Treatment began 11 d after tumor inoculation when the mean initial tumor volumes were 131 mm³ and 161 mm³ for studies with **9** and **10**, respectively. Compounds **9** and **10** were well-tolerated by the mice at all dose levels with no signs of clinical abnormalities or significant loss in body weight in the treated groups compared with the vehicle control group (Fig. 5 C and E). Significant levels of tumor

growth repression were observed for both probes with a similar in vivo efficacy pattern as **3**. Compound **9** exhibited the highest dose-dependent TGI, and tumor regression was achieved in the high dose group (150 mg/kg) by day 7. Tumor regression continued through the study and resulted in a 23% reduction in average tumor volume at the end of treatment. Furthermore, delayed tumor regrowth was observed during the observation period without additional doses. Compound **9** also achieved 59 and 84% TGI in the 50 and 100 mg/kg dose groups, respectively, which exceeded the TGI of **3** at the same dose levels via i.p. administration. Significant dose-related tumor control was apparent for **10** by exhibiting 51, 65, and 69% inhibition at 50, 100, and 150 mg/kg doses, respectively. The tumor exposure of **10** measured 1 h after the last dose in the 100 mg/kg dose group (11,468 \pm 3,595 ng/g) was similar to the 150 mg/kg dose (9,756 \pm 4,328 ng/g). This result suggests **10** may reach an oral absorption limit at the 100 mg/kg dose level, and the plasma exposure plateaued at the 100 mg/kg dose. Indeed, **9** exhibited a twofold higher kinetic aqueous solubility than **10**, which could be a major contributing factor to the nonlinear absorption pattern of **10** and explains the lack of dose-response between 100 and 150 mg/kg dose groups. In summary, both compounds exhibited excellent dose-dependent TGI without any sign of adverse effects. Despite a threefold higher unbound fraction of compounds **9** ($f_u = 1.3\%$) compared with **10** ($f_u = 0.4\%$) in mouse whole blood, both compounds showed

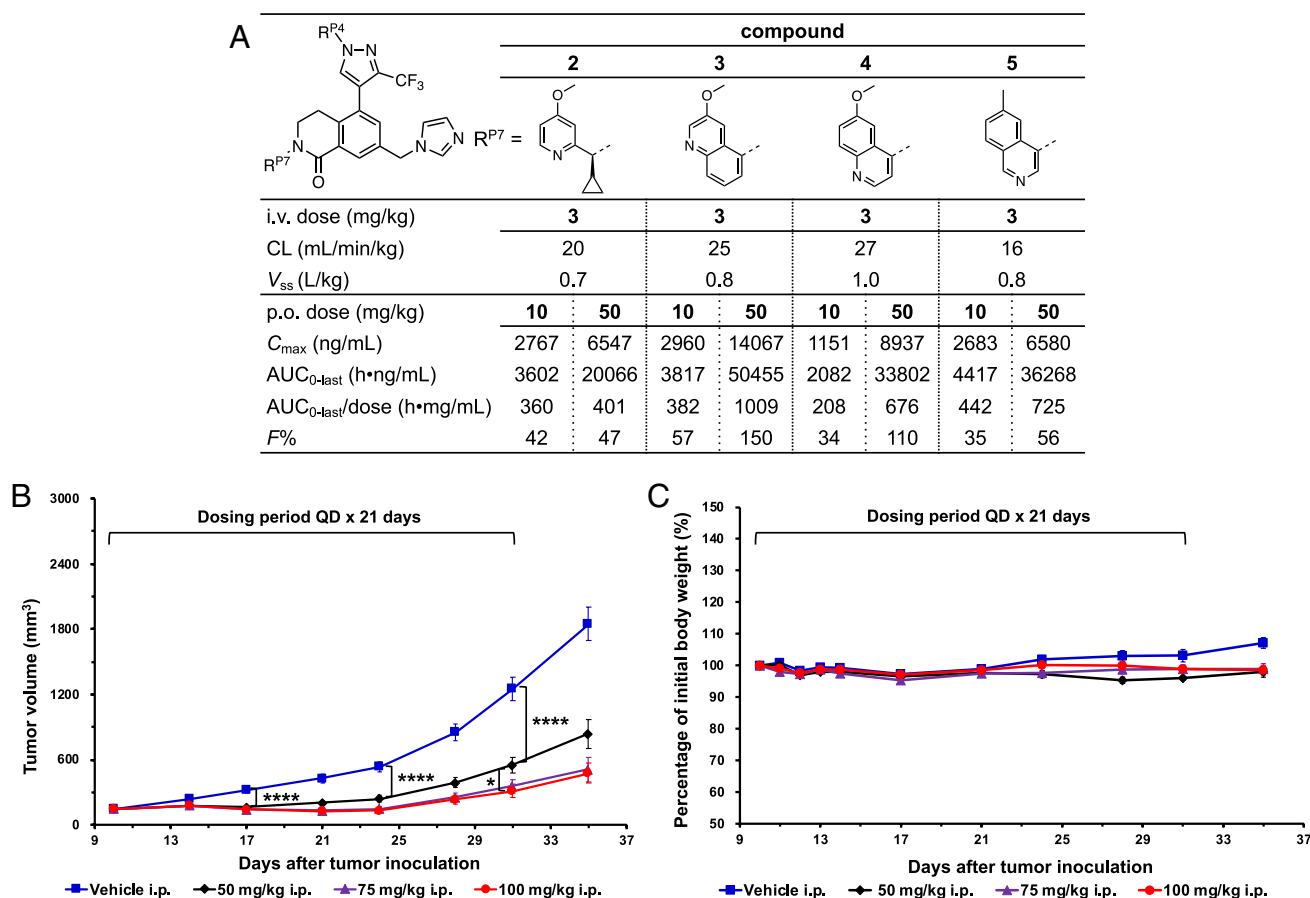


Fig. 4. Compound **3** demonstrated tumor growth suppression in an MV4:11 subcutaneous tumor xenograft model. (A) In vivo PK profiles of **2** to **5** in CD-1 mice ($n = 3$ per group) following a single dose of the indicated compound through i.v. (3 mg/kg) and p.o. (10 and 50 mg/kg) administration. CL, clearance; V_{ss} , volume of distribution at steady state; C_{max} , maximum plasma concentration; AUC_{0-last} , area under the plasma concentration-time curve ($t = 0$ -last timepoint); $AUC_{0-last}/dose$, dose-normalized area under the plasma concentration-time curve ($t = 0$ -last timepoint); $F\%$, oral bioavailability; R^{P4} is defined in Table 1. (B) The mean tumor volumes of MV4:11 subcutaneous xenografts in female BALB/c nude mice after QD treatment (21 d) with **3** via i.p. administration at the indicated doses. Treatment started 10 d after tumor inoculation as indicated. Tumor volumes were measured twice a week for the 3-wk study. (C) The percentage of mean body weight change from initial weights during the study at the indicated doses of **3**. Error bars represent the SEM, in (B) and (C) there were $n = 10$ mice per group. Statistical analysis was performed using an unpaired two-sided Student's t test in Excel. $*P < 0.05$, $**P < 0.01$, $***P < 0.001$, $****P < 0.0001$.

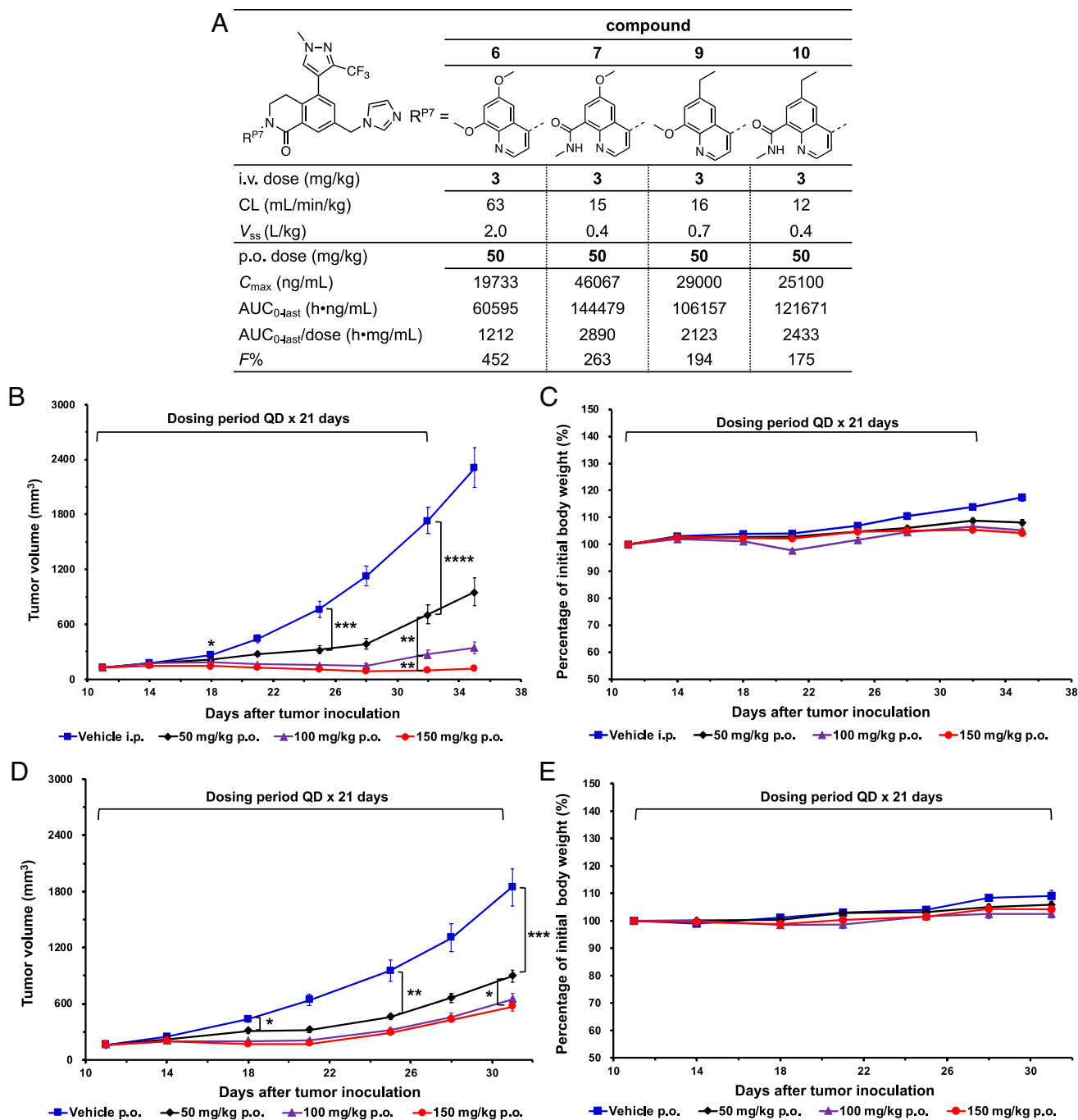


Fig. 5. Compounds **9** and **10** demonstrated antitumor effects in an MV4:11 subcutaneous tumor xenograft model. (A) In vivo PK profiles of **6**, **7**, **9**, and **10** in CD-1 mice ($n = 3$ per group) following a single dose of the indicated compound through i.v. (3 mg/kg) and p.o. (50 mg/kg) administration. (B) The mean tumor volumes of MV4:11 subcutaneous xenografts in female BALB/c nude mice after QD treatment (21 d) with **9** via p.o. administration at the indicated doses. Treatment started on day 11 and tumor volumes were recorded twice a week for the 3-wk study. (C) The percentage of mean body weight change from initial weights during the study at the indicated doses of **9**. (D) The mean tumor volumes of MV4:11 subcutaneous xenografts after QD treatment with **10** via p.o. administration. (E) The percentage of mean body weight change from initial weights following QD treatment with **10**. Error bars represent the SEM, in (B)–(E) there were $n = 10$ mice per group. Statistical analysis was performed using an unpaired two-sided Student's *t* test in Excel. * $P < 0.05$, ** $P < 0.01$, *** $P < 0.001$, **** $P < 0.0001$.

comparable in vivo efficacies in the 50 and 100 mg/kg dose groups, which suggests that the observed antitumor activity in the MV4:11 subcutaneous xenograft model may correlate better with the total exposure of the WIN-site inhibitor in tumor rather than the unbound fraction in plasma.

Compound 10 Retains On-Target Activity in Cells. To determine if the improvements in potency and oral bioavailability in **10** come at the expense of on-target activity, we profiled **10** against our earlier generation inhibitor C16, for which the mechanism of action in

cells has been extensively characterized (52). First, we compared **10** with C16 using our recently developed WDR5 target engagement assay that uses branched DNA technology (QuantiGene™) to measure transcript levels of five universal RPG targets of WDR5 (*RPL26*, *RPL32*, *RPL35*, *RPS14*, and *RPS24*) and two control RPGs (*RPS11* and *RPL14*), which are unresponsive to WIN-site inhibition (37, 44, 52). As expected (Fig. 6A and B), **10** and C16 show dose-dependent suppression of RPG transcripts in MV4:11 cells that is confined to the WDR5-targeted RPGs. Consistent with its improved antiproliferative activity in MV4:11 cells, **10**

is roughly fivefold more potent at suppressing these RPGs than C16 (dotted lines). As a result of RPG suppression, induction of a p53-mediated cellular response is observed in MLL-rearranged leukemia (44) and MYCN-amplified (37) cancer cell lines. Compound **10** induced similar levels of p53 at fivefold lower concentrations compared with C16 (Fig. 6C). Thus, **10** preserves the critical first (RPG suppression) and last (p53 induction) steps of the cellular response to WIN-site inhibition at lower doses.

To look more comprehensively at the response, we next performed RNA-sequencing (RNA-Seq) on MV4:11 cells treated for 72 h with 500 nM C16 or 100 nM **10** (SI Appendix, Fig. S4A). Here, we observed striking similarities between C16 and **10** in terms of the number of differentially expressed genes (Fig. 6D), the magnitude of the response (Fig. 6E and F), and the identity of the transcripts that are decreased (Fig. 6G) or increased (Fig. 6H) in response to both inhibitors. Importantly, the primary WDR5-bound RPG targets of WIN-site inhibition show an almost identical pattern of expression changes upon treatment with **10** as they do to C16 (Fig. 6I). For both inhibitors, transcriptional changes are largely confined to WDR5-bound RPGs, and within these genes both the magnitude of the change and the significance values are virtually identical for C16 and **10**. Consistent with the close similarities in gene expression profiles induced by both inhibitors, the nature of the impacted genes are also very similar and include the expected Gene Ontology categories (37, 44, 52). The suppressed genes are connected to translation, DNA replication, and the cell cycle (Fig. 6J). The induced genes are connected to p53, apoptosis, and autophagy (Fig. 6K). These categories and the similarities between C16 and **10** are further reinforced by Gene Set Enrichment Analysis (SI Appendix, Fig. S4B and C). Together these data show that **10** comports precisely with expectations for WIN-site inhibitor function in an MLL-rearranged cancer line and thus, despite major improvements in potency and in vivo action, retains on-target cellular activity.

PK and Safety Profile of Compound 10 in Rats. Prior to the safety assessment of WDR5 WIN-site inhibitors in rats, compounds **9** and **10** were evaluated in male Sprague–Dawley (SD) rats (SI Appendix, Fig. S5). Compounds **9** and **10** were dosed at 3 mg/kg by i.v. administration and display clearance rates of 53 and 40 mL/min/kg, respectively, which were significantly higher compared with the values obtained in mice (SI Appendix, Fig. S5C). Conversely, compound **10** showed 5.5-fold higher plasma exposure ($AUC_{0\text{--}last} = 55,664$ h ng/mL) compared with **9** ($AUC_{0\text{--}last} = 12,273$ h ng/mL) when dosed by oral administration at 50 mg/kg (SI Appendix, Fig. S5D). Although **9** demonstrated the most significant in vivo efficacy in the mouse xenograft model, it was not an ideal candidate for the safety study in rats due to limited systemic exposure by oral dosing. As observed by the PK studies in mice, the oral bioavailability of **10** in rats at the 50 mg/kg dose also exceeded 100%. This observation may be a result of more efficient absorption of **10** at the high dose due to saturation of clearance mechanisms. In addition, this may be caused by enterohepatic circulation (EHC). To determine if EHC contributes to the PK profile of **10** in rats, a single dose of **10** was administered orally at 50 mg/kg to bile duct cannulated (BDC) SD rats (SI Appendix, Fig. S6). Exposures of **10** in plasma, bile, and urine were monitored for 24 h. A small amount of the dosed parent compound was detected in bile (0.5%) and urine (0.4%) (SI Appendix, Fig. S6B). In addition, the total exposure of **10** ($AUC_{0\text{--}last} = 94,840$ h ng/mL) in the plasma of BDC rats was comparable to non-BCD rats ($AUC_{0\text{--}last} = 55,664$ h ng/mL) and mice ($AUC_{0\text{--}last} = 121,672$ h ng/mL) (SI Appendix, Fig. S6C).

This result suggests that nonhepatic clearance mechanisms in rats were minor contributors. Therefore, it is unlikely that EHC contributes to the PK profile of **10**. Furthermore, both species will likely exhibit similar exposures and clearance rates at high oral doses.

Based on the superior PK profile in rats, an exploratory 7-d dose-range-finding study in rats was conducted with **10** to determine the general safety and tolerability of small-molecule WDR5 WIN-site inhibitors. Three drug-treated groups of male SD rats were given oral doses of **10** at 50, 100 mg/kg QD, and 100 mg/kg twice daily (BID) for 7 d along with satellite groups at the same dose levels for toxicokinetic analysis (Fig. 7). Compound **10** exhibited a linear systemic exposure pattern at three dose levels on day 1 suggesting that this dosing strategy was effective. The PK profile of **10** on the final day of dosing was also determined and showed no significant difference in the peak plasma concentrations and oral exposures compared with day 1 (SI Appendix, Fig. S7B). The day 1 and 7 PK data suggest that **10** was completely cleared after each dose, and no noticeable dose accumulation was observed during the study. In the main study groups, **10** was well-tolerated, the rats in all treated groups gained weight, and no clinical abnormalities were reported during the study (SI Appendix, Table S1). On day 8, the rats were killed after blood collection for clinical pathology and subjected to gross necropsy, which showed no significant abnormalities. A dose-dependent mild reduction in spleen weight and thymus atrophy were noted among rats in the 100 mg/kg QD and BID groups and was expected to be reversible upon cessation of treatment. Blood chemistry results appeared to be within the normal ranges except for a mild increase of urea in the 100 mg/kg BID group and a decrease of creatine kinase in all groups independent of dose. Statistically significant hematological changes caused by **10** included a reduction of leukocytes, such as neutrophils (54%) and eosinophils (76%), in the high-dose group. However, leukocyte reduction is a common effect of anticancer therapy and is usually fully reversible. In short, **10** was well-tolerated in rats up to 100 mg/kg BID dose over the 7-d study without serious adverse effects. The demonstrated safety of WDR5 WIN-site inhibition further supports the development of this class of inhibitors toward clinical studies.

Discussion

WDR5 WIN-site inhibitors with enhanced on-target potency and PK profiles were discovered through the structure-based design and incorporation of bicyclic heteroaryl P_7 units. Compounds **3**, **9**, and **10** exhibit suitable PK profiles and demonstrated significant dose-dependent WDR5 inhibition-mediated tumor growth suppression in a mouse MV4:11 subcutaneous xenograft model. Importantly, **9** delivered the highest efficacy and achieved tumor regression in the disease model. Furthermore, we confirmed that the observed cellular activity achieved with **10** is a result of on-target WDR5 WIN-site inhibition. Our results indicate that it is critical to maintain a high level of WDR5 WIN-site occupancy in order to obtain a robust in vivo antitumor response by a small molecule agent. Therefore, a WIN-site inhibitor must exhibit extremely high on-target binding affinity and cellular potency, acceptable residence time in systemic circulation, and high oral bioavailability to be a practical therapeutic agent.

Potential WDR5 inhibition-mediated liabilities have been predicted by RNAi-mediated knockdown, which caused detrimental phenotypic responses in cells, such as altering H3K4 methylation status, to induce potential on-target toxicities (53–55). However, the blockade of the WIN-site by a small molecule inhibits only a

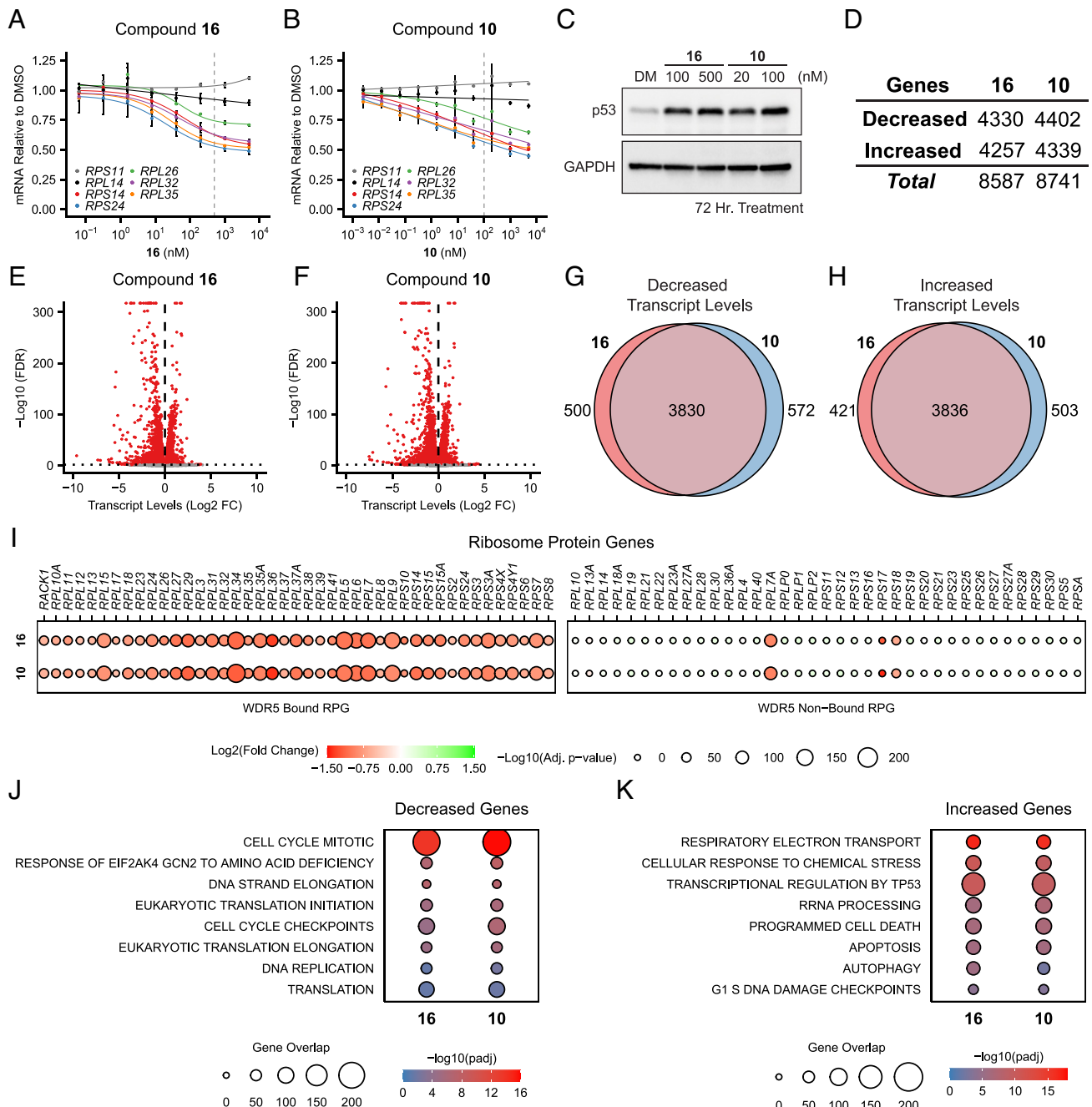


Fig. 6. Transcriptomic alterations in MV4:11 cells in response to compound **10** treatment. Transcript levels of representative WDR5-bound (color) and non-bound (grayscale) ribosomal protein genes in MV4:11 cells treated with serial dilutions of (A) C16 or (B) **10**. Dashed vertical lines indicate 500 nM C16 and 100 nM **10**. ($n = 3$, mean \pm SEM) (C) Western blot analysis of p53 in lysates from MV4:11 cells treated with indicated concentrations of dimethyl sulfoxide (DM), C16, or **10**. (D) Counts of differentially expressed genes in C16- and **10**-treated MV4:11 cells compared to dimethyl sulfoxide (DMSO) treatment as determined by RNA-Seq ($n = 4$, significant genes are those with False Discovery Rate (FDR) < 0.05). Transcript-level alterations of genes in MV4:11 cells treated with either (E) C16 or (F) **10** compared with DMSO treatment. Overlap of genes with significantly (G) decreased or (H) increased transcript levels in MV4:11 cells treated with C16 or **10** compared with DMSO treatment. (FDR < 0.05) (I) Transcript-level alterations of WDR5-bound and nonbound ribosome protein genes in C16- and **10**-treated MV4:11 cells. (J) Collection of significantly overrepresented Reactome gene set categories in genes with decreased transcript levels following C16- or **10**-treatment compared to DMSO treatment (FDR < 0.05). (K) As in (J) but for transcripts that increase in response to C16 or **10**.

specific subset of WDR5 functions and does not alter H3K4 methylation (49). Therefore, the true on-target liabilities associated with WDR5 WIN-site inhibition can only be assessed by a small-molecule inhibitor itself. All our in vivo probes are highly potent and selective WDR5 WIN-site inhibitors and showed excellent safety profiles in mice and rats under QD and BID dosing schedules.

WDR5 PROTACs have recently been reported and showed significant degradation of WDR5 in cells and in vivo efficacy in

a mouse MV4:11 xenograft model (48). The antitumor activities of WDR5 PROTACs would be mediated through the global reduction of WDR5 activities by depletion. Based on their mechanism of action, excessive degradation of WDR5 may elicit serious on-target-mediated adverse effects similar to RNAi-mediated knockdown, which remains to be determined using WDR5 PROTACs (56). Therefore, WIN-site inhibitors could offer advantages over WDR5 PROTACs for managing the potential on-target-mediated toxicity.

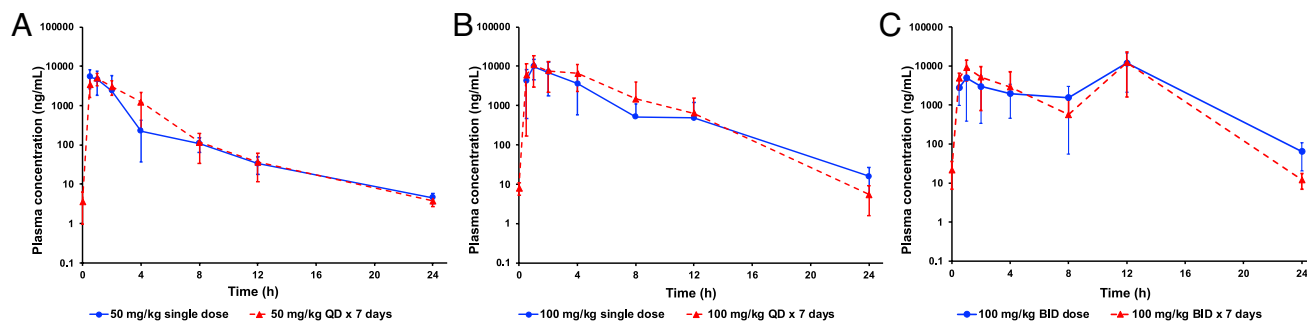


Fig. 7. Toxicokinetic analysis of compound **10** in rats. Compound **10** was administered orally (p.o.) to three groups of SD rats at doses of (A) 50 mg/kg QD (B) 100 mg/kg QD, and (C) 100 mg/kg BID for 7 d. Whole-blood samples were collected at the indicated time points up to 24 h following a single dose (blue solid lines) and after 7 d of dosing (red dashed lines). Error bars represent the SD, in (A)–(C) there were $n = 4$ rats per group.

Currently, we are in the process of redefining the mechanism of action, cancer vulnerability, and mechanism-based liabilities for WDR5 WIN-site inhibition using our probes. WIN-site inhibitors have shown strong inhibitory activity against MLL1 gene rearranged cancers. In addition, WDR5-bound MYC on RPGs can be indirectly targeted through the WIN site, which tethers WDR5 to chromatin (41, 44). Indeed, our WIN-site inhibitors displaced MYC from chromatin at protein synthesis genes, which was comparable to the disruption of the MYC–WDR5 complex by mutation of MYC (41, 44). This finding expands the potential utility of WDR5 WIN-site inhibitors to include MYC-up-regulated cancers. We continue to broaden the list of potential indications and identify reliable biomarkers for PD effects and patient selection criteria using our probes. Finally, our WDR5 WIN-site inhibitors successfully demonstrate robust *in vivo* anti-tumor efficacy with a clean safety profile and provide strong support for the clinical development of this class of inhibitors against a variety of cancers.

Materials and Methods

Compound Synthesis and Characterization. Detailed experimental methods for the synthesis of compounds **3** to **10** are provided in *SI Appendix, Materials and Methods*.

WDR5 Crystallization and X-ray Data Collection. Detailed experimental methods for the expression, purification, crystallization, data collection, and structure refinement for WDR5–ligand complexes are provided in *SI Appendix, Materials and Methods*.

In Vitro Assays and Experiments. Detailed experimental methods for the TR-FRET, cellular proliferation, kinetic solubility, mouse whole-blood protein binding, Western blotting, QuantiGene assay, RNA-Seq, and RNA-Sequencing bioinformatic analysis are provided in *SI Appendix, Materials and Methods*.

In Vivo Studies. Detailed experimental methods for the PK, efficacy, and safety studies in rodents are provided in *SI Appendix, Materials and Methods*. All animal studies were reviewed and approved by the Institutional Animal Care and Use Committee of Pharmaron, Inc. Animals were randomly assigned to various treatment groups, and scientists were not blinded to treatment groups. The number of animals included in the efficacy and safety studies was 10 and 4 per treatment group, respectively.

Statistical Analyses. Experimental data in Table 1 are presented as the mean \pm SD of ≥ 2 independent experiments. For *in vivo* efficacy studies, an unpaired two-sided Student's *t* test was performed with Excel to determine the statistical differences in the size of tumor xenografts. For the dose-range-finding safety study, treatment groups were compared with the vehicle control group and were judged as significant ($P < 0.05$) using one-way (ANOVA) performed with IBM® SPSS 16.0.

Data, Materials, and Software Availability. All data associated with this study are present in the paper or the [supporting information](#). Atom coordinates and

structure factors for WDR5–ligand complexes can be accessed in the PDB via the following accession code: [8E9F](#) (57), compound **10**. Genomic data sets have been deposited at the Gene Expression Omnibus (GEO) at [GSE203101](#) (58).

ACKNOWLEDGMENTS. We thank the Vanderbilt University High-Throughput Screening, Biomolecular NMR (NIH SIG Grant 1S-10RR025677-01), and Mass Spectrometry Research Center for providing compound management, NMR spectrometer, and high-resolution mass spectrometry services, respectively. The Vanderbilt University Medical Center Digestive Disease Research Center performed the Quantigene assays (NIH grant P30DK058404). RNA-Sequencing was performed by the VANTAGE Shared Resource which is supported by the CTSA Grant (RR024975), the Vanderbilt Ingram Cancer Center (VICC) (P30CA068485), the Vanderbilt Vision Center (P30EY08126), and the NIH and National Center for Research Resources (RR030956). B.C.G. was supported by the Brock Family Foundation. We gratefully acknowledge Drs. Elizabeth Glaze, Sandy Eldridge, and Joseph M. Covey from the Toxicology and Pharmacology Branch of the Division of Cancer Treatment and Diagnosis (DCTD) at the National Cancer Institute (NCI) for insightful discussions regarding the safety profile of the compounds. We express appreciation to Dr. Joel Morris and Mr. Donn Wishka from the Drug Synthesis and Chemistry Branch of DCTD for their assistance in compound scale-up. We thank Drs. Barbara Mroczkowski and Andrew Flint from DCTD for their project management support. We also thank all other contributing and supporting members of the DCTD, the NCI Chemical Biology Consortium, Curia Global, Inc., and Pharmaron, Inc. for their contributions to the project. This research used resources of the Advanced Photon Source, a US Department of Energy (DOE) Office of Science User Facility operated for the DOE Office of Science by Argonne National Laboratory under Contract No. DE-AC02-06CH11357. Use of the LS-CAT Sector 21 was supported by the Michigan Economic Development Corporation and the Michigan Technology Tri-Corridor (Grant 085P1000817). This work was generously supported in part by the NCI and NIH under Chemical Biology Consortium Contract No. HHSN26120080001E (to S.W.F.), VICC Support grant P30CA68485, NIH grant P50CA236733 (to S.W.F. and W.P.T.), NIH grant R01CA200709 (to W.P.T.), Vanderbilt University startup funds (to S.W.F.), Robert J. Kleberg, Jr., and Helen C. Kleberg Foundation (to W.P.T. and S.W.F.), NIH grants P30DK058404, RR024975, P30EY08126, RR030956, T32CA217834 (to B.C.G.), and the Brock Family Fellowship (to B.C.G.).

Author affiliations: ^aDepartment of Biochemistry, Vanderbilt University School of Medicine, Nashville, TN 37232-0146; ^bMolecular Design and Synthesis Center, Vanderbilt Institute of Chemical Biology, Vanderbilt University, Nashville, TN 37232-0142; ^cDepartment of Cell and Developmental Biology, Vanderbilt University School of Medicine, Nashville, TN 37232-0146; ^dDepartment of Biostatistics, Vanderbilt University Medical Center, Nashville, TN 37232-0004; ^eCenter for Quantitative Sciences, Vanderbilt University Medical Center, Nashville, TN 37232-0004; ^fDepartment of Medicine, Vanderbilt University Medical Center, Nashville, TN 37232-0011; ^gChemical Biology Laboratory, Center for Cancer Research, National Cancer Institute, Frederick, MD 21702-1201; ^hLeidos Biomedical Research, Frederick National Laboratory for Cancer Research, Frederick, MD 21701-4907; ⁱDepartment of Pharmacology, Vanderbilt University School of Medicine, Nashville, TN 37232-0146; and ^jDepartment of Chemistry, Vanderbilt University, Nashville, TN 37232-0146

Author contributions: K.B.T., W.J.M., G.M.S., W.P.T., T.L., and S.W.F. designed research; K.B.T., S.C., K.M.M., J.T., J.S., M.V.M., T.M.S., J.L.S., T.A.R., S.G., J.W., B.C.G., S.L.L., G.C.H., and Q.L. performed research; K.B.T., G.C.H., W.J.M., G.M.S., W.P.T., and T.L. analyzed data; W.P.T. and S.W.F. acquired funding; and K.B.T., G.C.H., W.P.T., T.L., and S.W.F. wrote the paper.

1. A. D. Guarnaccia, W. P. Tansey, Moonlighting with WDR5: A cellular multitasker. *J. Clin., Med.* **7**, 21 (2018).
2. J. F. Couture, E. Collazo, R. C. Trievel, Molecular recognition of histone H3 by the WD40 protein WDR5. *Nat. Struct. Mol. Biol.* **13**, 698–703 (2006).
3. D. Li, R. Roberts, WD-repeat proteins: Structure characteristics, biological function, and their involvement in human diseases. *Cell. Mol. Life Sci.* **58**, 2085–2097 (2001).
4. A. Patel, V. E. Vought, V. Dharmarajan, M. S. Cosgrove, A conserved arginine-containing motif crucial for the assembly and enzymatic activity of the mixed lineage leukemia protein-1 core complex. *J. Biol. Chem.* **283**, 32162–32175 (2008).
5. Z. Odho, S. M. Southall, J. R. Wilson, Characterization of a novel WDR5-binding site that recruits RbBP5 through a conserved motif to enhance methylation of histone H3 lysine 4 by mixed lineage leukemia protein-1. *J. Biol. Chem.* **285**, 32967–32976 (2010).
6. Z. Han *et al.*, Structural basis for the specific recognition of methylated histone H3 lysine 4 by the WD-40 protein WDR5. *Mol. Cell* **22**, 137–144 (2006).
7. X. Chen *et al.*, Targeting WD repeat-containing protein 5 (WDR5): A medicinal chemistry perspective. *J. Med. Chem.* **64**, 10537–10556 (2021).
8. Y. Li *et al.*, Structural basis for activity regulation of MLL family methyltransferases. *Nature* **530**, 447–452 (2016).
9. B. P. Jain, S. Pandey, WD40 repeat proteins: Signalling scaffold with diverse functions. *Protein J.* **37**, 391–406 (2018).
10. X. Chen *et al.*, Upregulated WDR5 promotes proliferation, self-renewal and chemoresistance in bladder cancer via mediating H3K4 trimethylation. *Sci. Rep.* **5**, 8293 (2015).
11. X. Dai *et al.*, WDR5 expression is prognostic of breast cancer outcome. *PLoS One* **10**, e0124964 (2015).
12. X. Tan *et al.*, PI3K/AKT-mediated upregulation of WDR5 promotes colorectal cancer metastasis by directly targeting ZNF407. *Cell Death Dis.* **8**, e2686 (2017).
13. W. Sun, F. Guo, M. Liu, Up-regulated WDR5 promotes gastric cancer formation by induced cyclin D1 expression. *J. Cell. Biochem.* **119**, 3304–3316 (2018).
14. A. Carugo *et al.*, In vivo functional platform targeting patient-derived xenografts identifies WDR5-Myc association as a critical determinant of pancreatic cancer. *Cell Rep.* **16**, 133–147 (2016).
15. R. Malek *et al.*, TWIST1-WDR5-Hottip regulates Hoxa9 chromatin to facilitate prostate cancer metastasis. *Cancer Res.* **77**, 3181–3193 (2017).
16. P. T. Tran *et al.*, A twist1-MLL-WDR5-HOTTIP complex regulates HOXA9 chromatin to facilitate metastasis of prostate cancer. *Int. J. Radiat. Oncol.* **90**, S177 (2014).
17. Y. Sun *et al.*, WDR5 supports an N-Myc transcriptional complex that drives a protumorigenic gene expression signature in neuroblastoma. *Cancer Res.* **75**, 5143–5154 (2015).
18. Y. Wu *et al.*, Overexpression of WD repeat domain 5 associates with aggressive clinicopathological features and unfavorable prognosis in head neck squamous cell carcinoma. *J. Oral Pathol. Med.* **47**, 502–510 (2018).
19. Z. Cui *et al.*, Effect of high WDR5 expression on the hepatocellular carcinoma prognosis. *Oncol. Lett.* **15**, 7864–7870 (2018).
20. Z. Ge *et al.*, WDR5 high expression and its effect on tumorigenesis in leukemia. *Oncotarget* **7**, 37740–37754 (2016).
21. Z. Ge, E. Song, J. Li, S. Dovat, C. Song, Clinical significance of WDR5 high expression and its effect on tumorigenesis in adult leukemia. *Blood* **126**, 3657 (2015).
22. T. F. Smith, C. Gaitatzes, K. Saxena, E. J. Neer, The WD repeat: A common architecture for diverse functions. *Trends Biochem. Sci.* **24**, 181–185 (1999).
23. C. U. Stirnimann, E. Petsalaki, R. B. Russell, C. W. Muller, WD40 proteins propel cellular networks. *Trends Biochem. Sci.* **35**, 565–574 (2010).
24. C. Xu, J. Min, Structure and function of WD40 domain proteins. *Protein Cell* **2**, 202–214 (2011).
25. M. Wu, H. B. Shu, MLL1/WDR5 complex in leukemogenesis and epigenetic regulation. *Chin. J. Cancer* **30**, 240–246 (2011).
26. A. Patel, V. Dharmarajan, M. S. Cosgrove, Structure of WDR5 bound to mixed lineage leukemia protein-1 peptide. *J. Biol. Chem.* **283**, 32158–32161 (2008).
27. J. L. Hess, MLL: A histone methyltransferase disrupted in leukemia. *Trends Mol. Med.* **10**, 500–507 (2004).
28. V. Dharmarajan, J.-H.H. Lee, A. Patel, D. G. Skalnik, M. S. Cosgrove, Structural basis for WDR5 interaction (Win) motif recognition in human SET1 family histone methyltransferases. *J. Biol. Chem.* **287**, 27275–27289 (2012).
29. N. L. Alicia-Velázquez *et al.*, Targeted disruption of the interaction between WD-40 repeat protein 5 (WDR5) and mixed lineage leukemia (MLL)/SET1 family proteins specifically inhibits MLL1 and SET1A methyltransferase complexes. *J. Biol. Chem.* **291**, 22357–22372 (2016).
30. E. R. Aho, A. M. Weissmiller, S. W. Fesik, W. P. Tansey, Targeting WDR5: A WINning anti-cancer strategy? *Epigenetics Insights* **12**, 1–5 (2019).
31. L. R. Thomas, C. M. Adams, S. W. Fesik, C. M. Eischen, W. P. Tansey, Targeting MYC through WDR5. *Mol. Cell. Oncol.* **7**, 1709388 (2020).
32. L. R. Thomas *et al.*, Interaction with WDR5 promotes target gene recognition and tumorigenesis by MYC. *Mol. Cell* **58**, 440–452 (2015).
33. L. R. Thomas *et al.*, Interaction of the oncoprotein transcription factor MYC with its chromatin cofactor WDR5 is essential for tumor maintenance. *Proc. Natl. Acad. Sci. U.S.A.* **116**, 25260–25268 (2019).
34. K. Lu, H. Tao, X. Si, Q. Chen, The histone H3 lysine 4 presenter WDR5 as an oncogenic protein and novel epigenetic target in cancer. *Front. Oncol.* **8**, 502 (2018).
35. H. Karatas *et al.*, Discovery of a highly potent, cell-permeable macrocyclic peptidomimetic (MM-589) targeting the WD repeat domain 5 protein (WDR5)-mixed lineage leukemia (MLL) protein-protein interaction. *J. Med. Chem.* **60**, 4818–4839 (2017).
36. F. Grebien *et al.*, Pharmacological targeting of the WDR5-MLL interaction in C/EBP α -N-terminal leukemia. *Nat. Chem. Biol.* **11**, 571–578 (2015).
37. A. F. Bryan *et al.*, WDR5 is a conserved regulator of protein synthesis gene expression. *Nucleic Acids Res.* **48**, 2924–2941 (2020).
38. F. Cao *et al.*, Targeting MLL1 H3K4 methyltransferase activity in mixed-lineage leukemia. *Mol. Cell* **53**, 247–261 (2014).
39. D. D. Li *et al.*, Structure-based design and synthesis of small molecular inhibitors disturbing the interaction of MLL1-WDR5. *Eur. J. Med. Chem.* **118**, 1–8 (2016).
40. X. Zhang *et al.*, Piribedil disrupts the MLL1-WDR5 interaction and sensitizes MLL-rearranged acute myeloid leukemia (AML) to doxorubicin-induced apoptosis. *Cancer Lett.* **431**, 150–160 (2018).
41. J. Tian *et al.*, Discovery and structure-based optimization of potent and selective WD repeat domain 5 (WDR5) inhibitors containing a dihydroisoquinoline bicyclic core. *J. Med. Chem.* **63**, 656–675 (2020).
42. M. Getlik *et al.*, Structure-based optimization of a small molecule antagonist of the interaction between WD repeat-containing protein 5 (WDR5) and mixed-lineage leukemia 1 (MLL1). *J. Med. Chem.* **59**, 2478–2496 (2016).
43. F. Wang *et al.*, Discovery of potent 2-Aryl-6,7-dihydro-5H-pyrrolo[1,2-a]imidazoles as WDR5-WIN-site inhibitors using fragment-based methods and structure-based design. *J. Med. Chem.* **61**, 5623–5642 (2018).
44. E. R. Aho *et al.*, Displacement of WDR5 from chromatin by a WIN site inhibitor with picomolar affinity. *Cell Rep.* **26**, 2916–2928 (2019).
45. K. B. Teuscher *et al.*, Discovery of potent orally bioavailable WD repeat domain 5 (WDR5) inhibitors using a pharmacophore-based optimization. *J. Med. Chem.* **65**, 6287–6312 (2022).
46. A. Tsherniak *et al.*, Defining a cancer dependency map. *Cell* **170**, 564–576 (2017).
47. E. R. McDonald III, *et al.*, Project DRIVE: A compendium of cancer dependencies and synthetic lethal relationships uncovered by large-scale deep RNAi screening. *Cell* **170**, 577–592 (2017).
48. X. Yu *et al.*, A selective WDR5 degrader inhibits acute myeloid leukemia in patient-derived mouse models. *Sci. Transl. Med.* **13**, eabj1578 (2021).
49. A. J. Siladi *et al.*, WIN site inhibition disrupts a subset of WDR5 function. *Sci Rep* **12**, 1848 (2022).
50. H. Karatas, E. C. Townsend, D. Bernard, Y. Dou, S. Wang, Analysis of the binding of mixed lineage leukemia 1 (MLL1) and histone 3 peptides to WD repeat domain 5 (WDR5) for the design of inhibitors of the MLL1–WDR5 interaction. *J. Med. Chem.* **53**, 5179–5185 (2010).
51. T. Lee *et al.*, WDR5 inhibitors and modulators. (Vanderbilt University, 2021) <https://patentscope.wipo.int/search/en/detail.jsf?docId=WO2021092525>. 14 May 2021.
52. A. C. Florian *et al.*, Synergistic action of WDR5 and HDM2 inhibitors in SMARCB1-deficient cancer cells. *NAR. Cancer* **4**, zcac007 (2022).
53. J. Zhu *et al.*, Gain-of-function P53 mutants co-opt chromatin pathways to drive cancer growth. *Nature* **525**, 206–211 (2015).
54. B. K. Nielsen *et al.*, WDR5 supports colon cancer cells by promoting methylation of H3K4 and suppressing DNA damage. *BMC Cancer* **18**, 673 (2018).
55. S. Punzi *et al.*, WDR5 inhibition halts metastasis dissemination by repressing the mesenchymal phenotype of breast cancer cells. *Breast Cancer Res.* **21**, 123 (2019).
56. K. Moreau *et al.*, Proteolysis-targeting chimeras in drug development: A safety perspective. *Br. J. Pharmacol.* **117**, 1709–1718 (2020).
57. T. A. Rietz, S. W. Fesik, WD repeat-containing protein 5 complexed with 4-(7-((1Himidazol-1-yl)methyl)-5-(1-methyl-3-(trifluoromethyl)-1H-pyrazol-4-yl)-1-oxo-3,4-dihydroisoquinolin-2(1H)-yl)-6-ethyl-N-methylquinoline-8-carboxamide (compound 10) RCSB PDB (ProteinData Bank <https://www.rcsb.org/structure/8E9F>). Deposited 26 August 2022.
58. W. P. Tansey, S. Goswami, G. C. Howard, J. Wang, Q. Liu Structure-Based Discovery of Potent WD Repeat Domain 5 Inhibitors that Demonstrate Efficacy and Safety in Preclinical Animal Models. Gene Expression Omnibus <https://www.ncbi.nlm.nih.gov/geo/query/acc.cgi?acc=GSE203101>. Deposited 16 May 2022.